IEPC-03-0056

NOZZLE SHAPE EFFECTS ON VELOCITY DISTRIBUTION IN AN MPD ARCJET

[*]Kiyoshi KINEFUCHI and [†]Kyoichiro TOKI
Institute of Space and Astronautical Science, Kanagawa, JAPAN

[‡]Ikkoh FUNAKI
Institute of Engineering Mechanics and Systems, University of Tsukuba, Ibaraki, JAPAN

Abstract

Both experimental velocimetry with plasma diagnostics and numerical analysis in the discharge chamber of a two-dimensional magnetoplasmadynamic (2D-MPD) arcjet were conducted in order to investigate the acceleration mechanisms in the case of hydrogen propellant. In the experiment, we estimated the velocity and temperature of the neutral atoms from the laser absorption profile, ion velocity and Mach number from TOF and Mach probe method respectively and electron temperature and plasma density from the Langmuir probe method. Results using two types of anodes, one being a conventional flared type anode and the other being a converging-diverging (C-D) type anode, were compared. It was found that there is region where ion-neutral velocity slip takes place and the acceleration of the neutral particles is not high enough. This phenomenon is the factor that decreases thrust performance and is due to the fact that the number of ion-neutral momentum transfer collisions is not high enough, so that neutrals cannot accelerate sufficiently. Comparing two types of anodes, the performance of the configuration employing a C-D anode was found to be relatively high especially at low Isp operation. This was explained by considering that the ion-neutral couple region was wider in this case, or, in other words, the region where velocity slip takes place was relatively small. However, at high Isp operation, flared anode is superior because electromagnetic acceleration is dominant in this anode shape.

Introduction

Quasi-steady MPD arcjet systems have been flight-tested on several spacecraft including the Japanese Space Flyer Unit (SFU) developed by Institute of Space and Astronautical Science (ISAS)[1]. However, MPD arcjet have not reached practical stage because of their low thrust efficiency and very high-required input power. For MPD arcjets to reach maturity the physical processes taking place in the discharge chamber must be first of all clearly understood and especially internal velocity distribution is a key factor. In this study, both experimental velocimetry with plasma diagnostics and numerical analysis in the discharge chamber has been performed concerning two types of anodes. The main objective is to grasp a firm understanding of the acceleration process inside MPD arcjets, so as to produce guidelines for improving their thrust performance.

Experimental Apparatus and Procedures

2D-MPD arcjet

The investigated 2D-MPD arcjet (Fig. 1) provides a nearly two-dimensional flowfield with 16 discharge channels, each of which has a centered 2 % Th-W cathode and two Cu anodes. Two types of anodes are fabricated and the geometries are shown in Fig. 2. One is simple flared type anode and the other is converging-diverging (C-D) type anode. The thruster head was placed inside a stainless-steel vacuum tank of 0.8 m diameter and 2.0 m length, which was evacuated to less than 2 mPa before each firing.

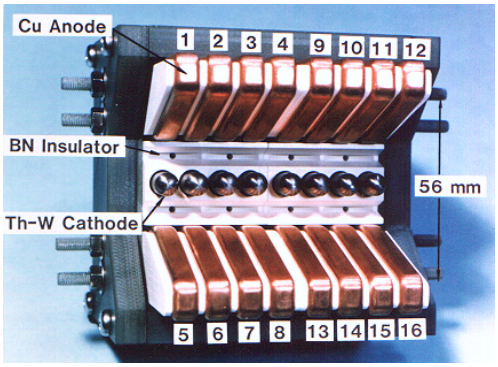

Fig. 1 2D-MPD arcjet.

[*] Graduate Student, University of Tokyo
[†] Professor, Member AIAA/JSASS
[‡] Assistant Professor, Member AIAA/JSASS

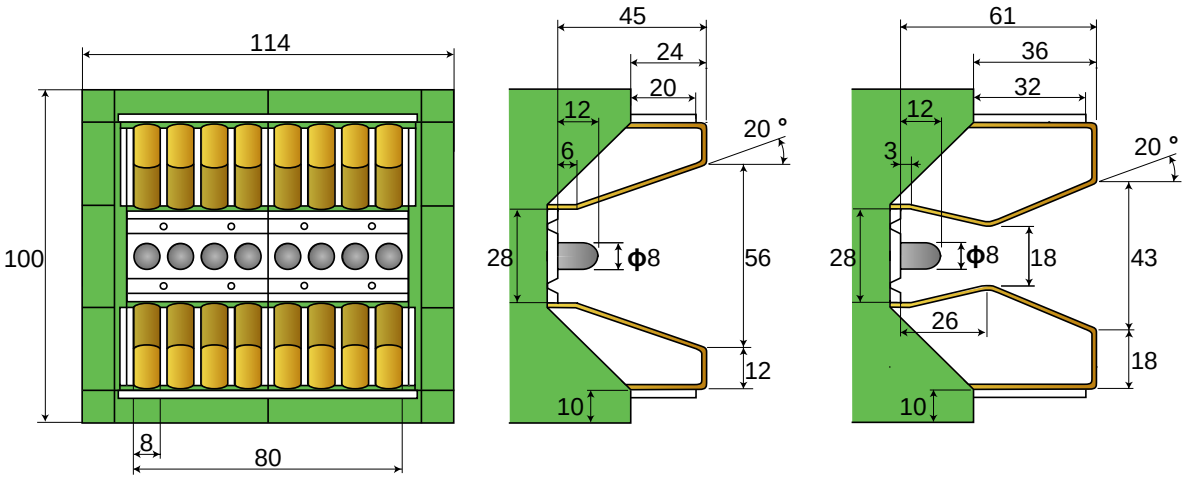

Fig. 2 Geometries of 2D-MPD arcjet.

The fast-acting valve (FAV)[2] allowed us to feed in gaseous propellants featuring a rectangular waveform signal. The FAV simultaneously opens and closes eight valves, and the gas in the reservoir flows through choked orifices of 1.2 mm in diameter. A gas pulse of about 5 ms duration was then introduced into the chamber by eight gas ports located between the anodes and the cathodes.

After the gas pulse reaches its quasi-steady state, the ignitron of a pulse-forming network (PFN)[3] is triggered. The PFN supplies the discharge current with a 0.1 ms flat-topped waveform in the quasi-steady mode. All of the performance and plasma parameters were measured during this 0.1 ms quasi-steady state time interval. Once the PFN is triggered, a charging voltage of at least 2 kV automatically introduces the arc breakdown. Channel-to-channel discharge uniformity was achieved by forcing the total discharge current through 16 equally divided 1.25 Ω resistors. As for the propellant, H_2 was specified and adjustment of the reservoir pressure resulted in control of the mass flow rate.

Laser absorption spectroscopy

The laser beam corresponding to the difference between the energy level of the particle is absorbed by the particle[4] and the absorption spectrum has the information of the plasma properties as shown Fig. 3. The absorption ratio is defined as $1-(I/I_0)$, where I is absorbed laser intensity and I_0 is incident laser intensity.

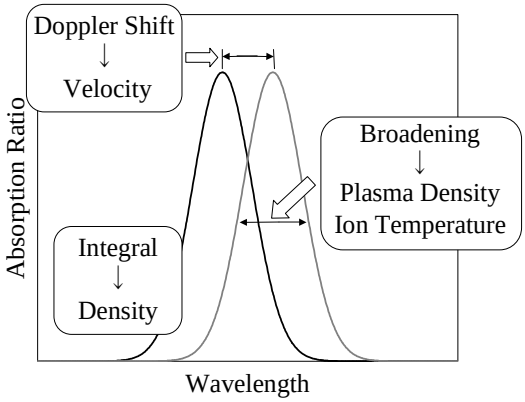

Fig. 3 Relationship between spectrum and plasma parameters.

When the particle has the velocity component whose direction is same as the laser path, the Doppler shift corresponding to this velocity takes place. Based on this, the particle velocity u is obtained from this Doppler shift frequency $\Delta\nu$ from the following expression:

$$u = \frac{\lambda_0 \Delta\nu}{\sin\theta_1 - \sin\theta_2} \qquad (1)$$

where λ_0 is center wavelength of the laser and θ_1 and θ_2 is incident angle of the laser to plasma.

The broadening of spectrum contains the information concerning the plasma density and the heavy particle temperature[5]. The heavy particle temperature T is shown as follows,

$$T = \frac{A(\lambda_0 \nu_D)^2}{8 \ln 2 R} \qquad (2)$$

where ν_D is FWHM of Doppler broadening, A is molecular weight and R is gas constant. Two types of broadening are separated fitting the Voigt profile to the spectrum[6].

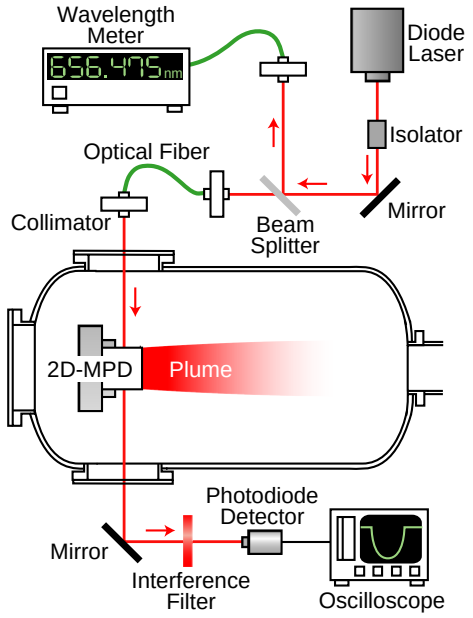

Fig. 4 Laser absorption spectroscopy system.

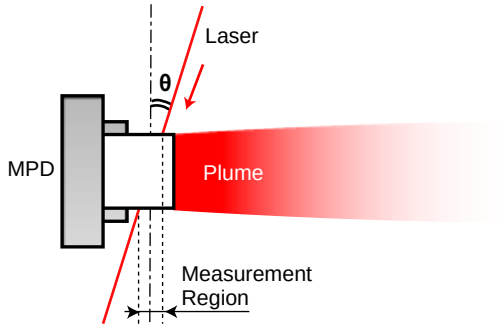

Fig. 5 Incident laser angle for the Doppler shift measurement.

The laser absorption spectroscopy system is shown Fig. 4. A semiconductor laser was adopted as the laser source and the absorption intensity was measured using a photodiode detector. Since there were no devices in our laser system to sweep the laser wavelength in a range wider than the spectrum broadening of hydrogen during the 0.1 ms quasi-steady time interval, the following procedure was performed:

1) Modulation the laser frequency
2) Firing of the 2D-MPD arcjet
3) Acquisition of the absorption intensity
4) Repetition of steps 1 through 3 until the spectrum was obtained.

The wavelength of the laser was modulated around 656 nm (Balmer alpha line of hydrogen atom). Thus the atoms are excited from principal quantum number 2 through 3 by the laser beam. In order to obtain the Doppler shift, the laser beam was directed at an incident angle θ relative to the 2D-MPD arcjet normal axis, as can be seen in Fig. 5. Comparing the two spectra for the incident angles θ_1 and θ_2 , the Doppler shift was estimated and from equation (1) the axial velocity was calculated. In this experiment, θ_1 and θ_2 were set at +10 and -10 degrees respectively, so that the measurement region in the chamber is 1.4cm.

Langmuir probe method

The probe measurement system is shown in Fig. 6. The probe, 0.3 mm in diameter tungsten wire covered by 1.0 mm in diameter insulator, inserted perpendicular to the flow. In order to sweep the voltage during 100 μs quasi-steady state, high frequency triangle shape voltage wave was applied to the probe. Because the magnetic field strength in the upstream region is approximately 0.1 T, electrons may be affected from the magnetic field strongly. So the plasma density was estimated from ion saturation current.

Mach probe method

Because we employ the hydrogen as propellant, spectroscopic methods cannot be applied for the ion velocity measurement. Therefore, Mach probe method was adopted. Ion Mach number M_i can be expressed as[7][8][9]:

$$M_i = \kappa \frac{J_{para}}{J_{perp}} \quad (M_i > 1) \tag{3}$$

$$M_i = \left[-\frac{1}{\ln \kappa} \ln\left(\frac{J_{para}}{J_{perp}} \right) \right]^{-\ln \kappa} \quad (M_i < 1) \tag{4}$$

where J_{para} is ion saturation current parallel to the flow, J_{perp} is ion saturation current perpendicular to the flow and κ is a coefficient depending on the temperature ratio T_i/T_e [7], where T_i is ion

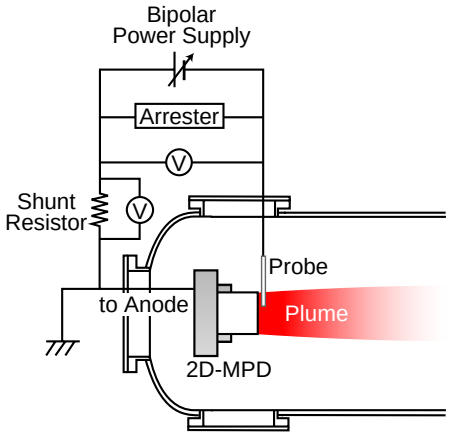

Fig. 6 Probe measurement system.

temperature and T_e is electron temperature. The Mach probe measurement was conducted using same system as Langmuir probe measurement (Fig. 6).

TOF (Time Of Flight)

The ion velocity was measured using a time-of-flight (TOF) method. Fig. 7 shows the concept of our TOF[11]. When plasma goes through between terminals, the capacitor provides the current to the circuit during discharge duration. Comparing the two current waveforms, we can obtain the ion velocity directly. The experimental system is shown in Fig. 8. The interval of two TOF probes is 1.0 cm. This method is applicable to the region where there is no discharge current. So in our experiment, this measurement was conducted only at the thruster exit on the centerline.

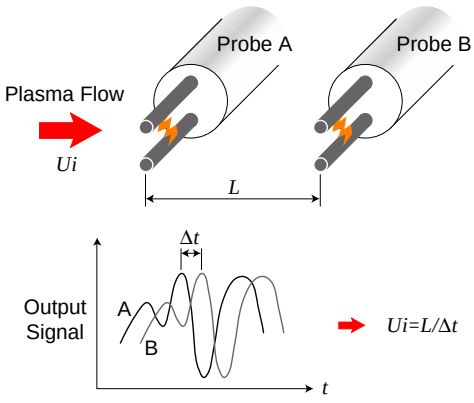

Fig. 7 Concept of TOF.

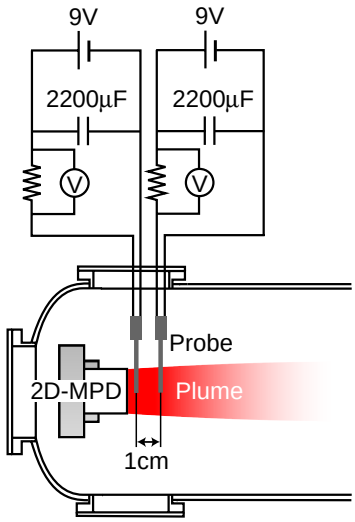

Fig. 8 TOF system.

Experimental Results

The experimental conditions and basic performances of flared anode and C-D anode are given in Table 1. The discharge current and the mass flow rate are same in both cases. The specific impulse of flared anode is superior to C-D anode. However, because the discharge current path in C-D anode is shorter than that of flared anode, the discharge voltage is relatively low in the case of C-D anode such that the thrust efficiencies are almost same magnitude. The current waveform shown in Fig. 9 has approximately 100 μs quasi steady state and discharge period is about 500 μs. The absorption spectrum is shown in Fig. 10 and Doppler shift is observed. Figure 11 is the characteristic example of Langmuir probe method. A TOF signal example (Fig. 12) shows straightforward relationship between two signals.

Figure 13 is ion velocity on the centerline by TOF method. The distributions of measured parameters in the flared anode and C-D anode are shown in Figs. 14 and 15, respectively. The axial velocity distribution calculated from the Doppler shift using equation (1), atom temperature is estimated from equation (2), plasma density and electron temperature were estimated from Langmuir probe characteristic. The ion Mach number was estimated using equations (3) and (4).

Table 1 Basic performance.

	Flared	C-D
Propellant	H_2	H_2
Mass flow rate	0.65 g/s	0.65 g/s
Discharge current	13 kA	13 kA
Discharge voltage	117 V	91 V
Specific impulse	4240 s	3770 s
Efficiency	37 %	38 %

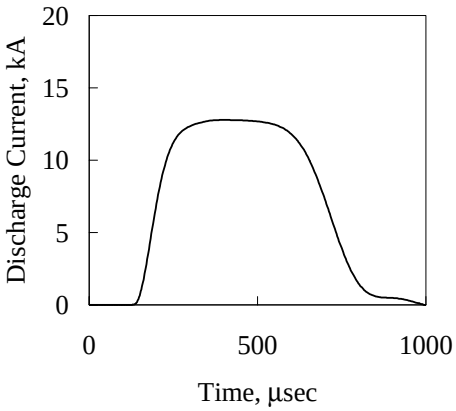

Fig. 9 Current waveform.

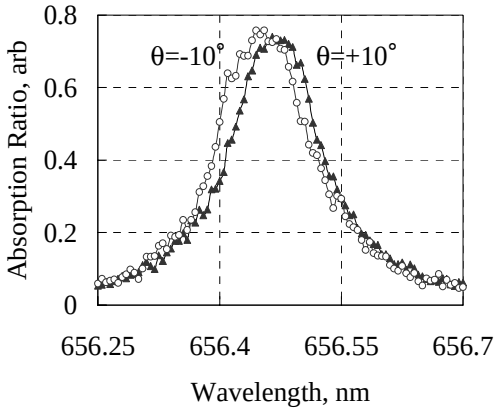

Fig. 10 Absorption Spectrum example.

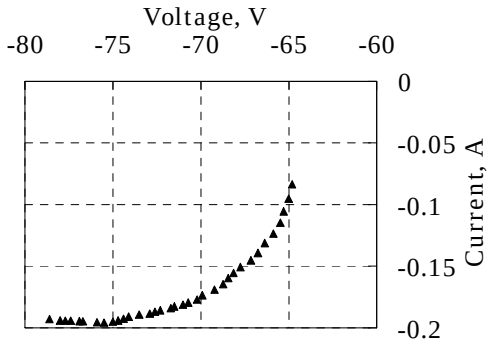

Fig. 11 Probe characteristic example.

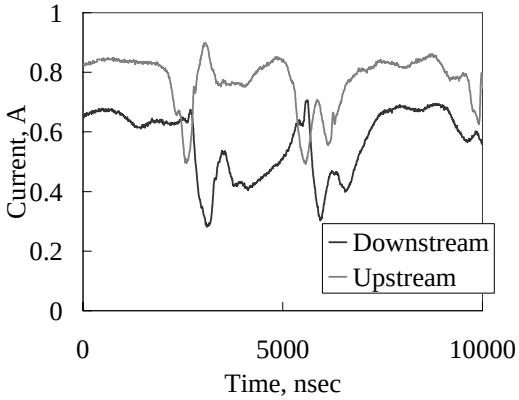

Fig. 12 TOF signal example.

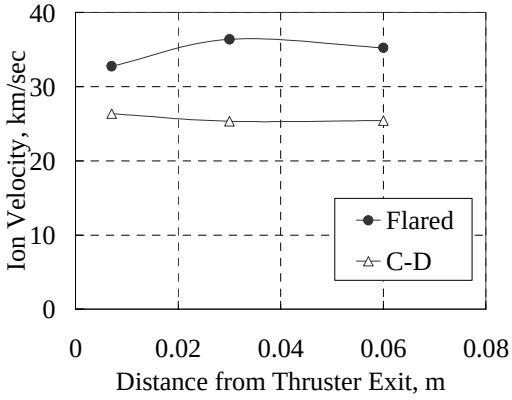

Fig. 13 TOF results.

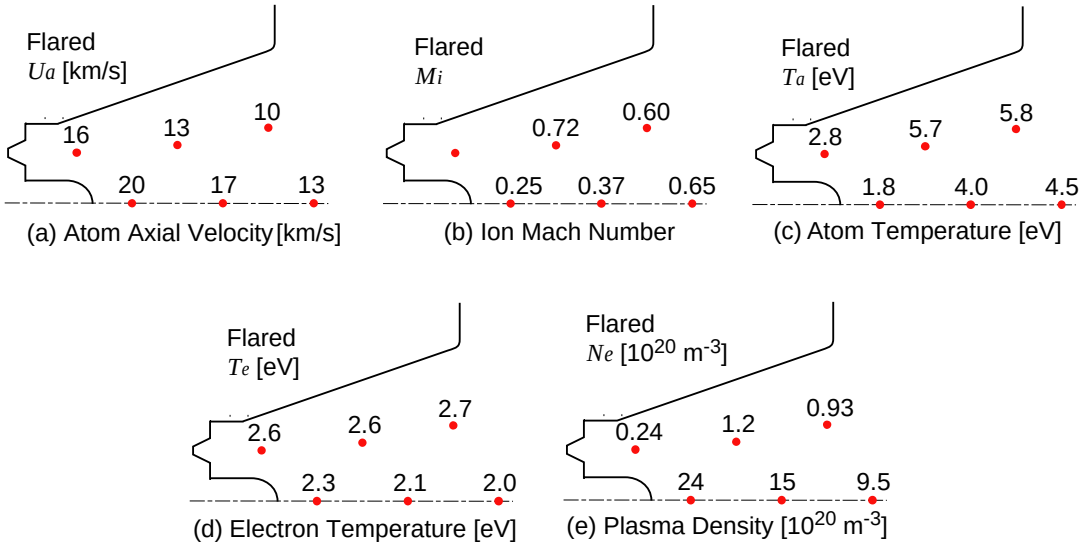

Fig. 14 Experimental Results in flared anode.

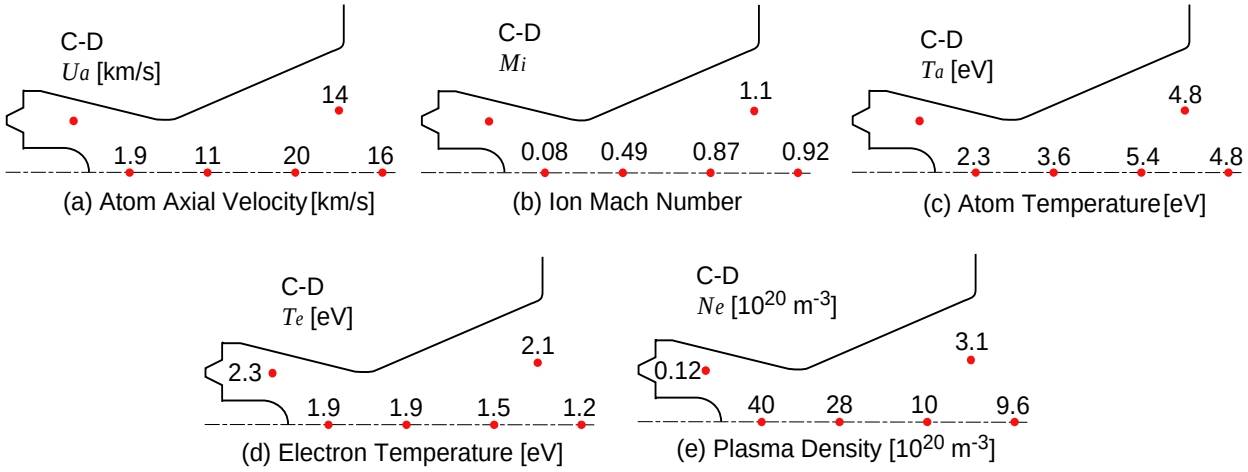

Fig. 15 Experimental Results in C-D anode.

Numerical Analysis

In order to enable more complete discussion of the experimental results, a quasi-one-dimensional numerical code solving MHD equations was developed[12]. Figure 16 shows the numerical model. Solving the magnetic field equation, we assume the existence of virtual cathode. For fluid equations, the calculations were conducted with same boundary conditions and electrode shapes as in the experiment. The Hall effect and dissociation process of hydrogen are neglected and viscosity and thermal conductivity are considered. Under such assumptions, the MHD equations can be written as follows.

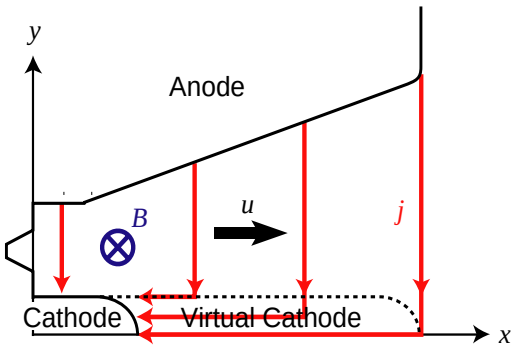

Fig. 16 Numerical model.

Global continuity: $$\frac{\partial \rho A}{\partial t}+\frac{\partial \rho u A}{\partial x}=0 \tag{5}$$

Ion continuity: $$\frac{\partial \rho_i A}{\partial t}+\frac{\partial \rho_i u A}{\partial x}=AS_{ci} \tag{6}$$

Neutral momentum: $$\frac{\partial \rho_n u_n A}{\partial t}+\frac{\partial \rho_n u_n^2 A}{\partial x}+A\frac{\partial p_n}{\partial x}=AS_{mn} \tag{7}$$

Ion momentum: $$\frac{\partial \rho_i u_i A}{\partial t}+\frac{\partial \rho_i u_i^2 A}{\partial x}+A\frac{\partial p_i}{\partial x}=AS_{mi} \tag{8}$$

Neutral energy: $$\frac{\partial \rho_n e_n A}{\partial t}+\frac{\partial \rho_n e_n u_n A}{\partial x}+p_n\frac{\partial u_n A}{\partial x}=AS_{en} \tag{9}$$

Ion energy: $$\frac{\partial \rho_i e_i A}{\partial t}+\frac{\partial \rho_i e_i u_i A}{\partial x}+p_i\frac{\partial u_i A}{\partial x}=AS_{ei} \tag{10}$$

Electron energy: $$\frac{\partial \rho_e e_e A}{\partial t}+\frac{\partial \rho_e e_e u_e A}{\partial x}+p_e\frac{\partial u_e A}{\partial x}=AS_{ee} \tag{11}$$

Magnetic field: $$d_{ac}\frac{\partial B}{\partial t}+\frac{\partial u_i B d_{ac}}{\partial x}-d_{ac}\frac{\partial B}{\partial x}\frac{\partial}{\partial x}\left(\frac{1}{\sigma\mu_0}\right)-\frac{1}{\sigma\mu_0}\frac{\partial B}{\partial x}\frac{dd_{ac}}{dx}=d_{ac}\frac{1}{\sigma\mu_0}\frac{\partial^2 B}{\partial x^2} \tag{12}$$

Where, $e_s=c_{vs}T_s$ $(s=a,i,e)$ and $d_{ac}(x)=y_{anode}(x)-y_{cathode}(0)$. Concerning source terms S, the detailed discussion was appeared in reference [7]. The computation results are show in Figs. 17 and 18.

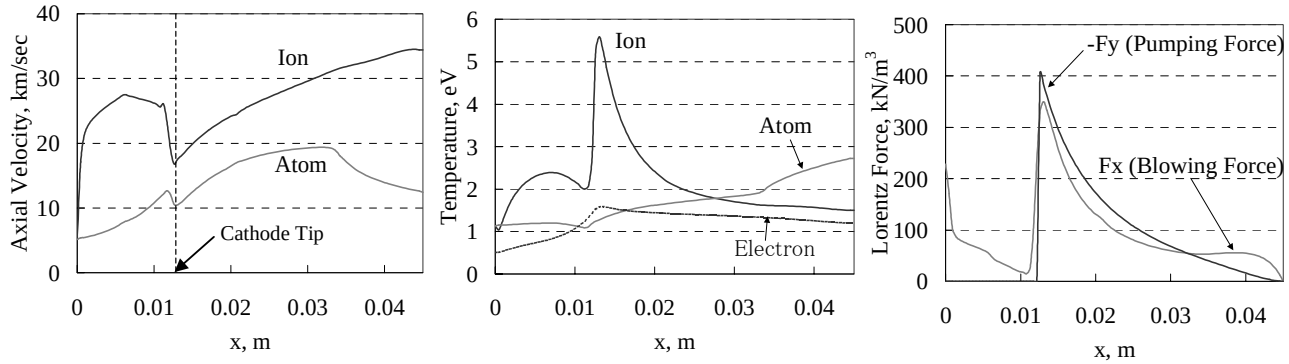

Fig. 17 Computational results of flared anode.

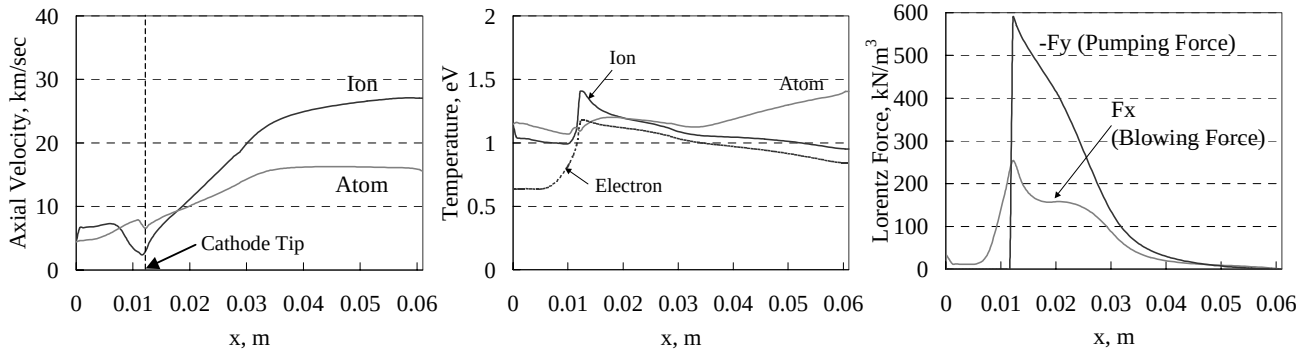

Fig. 18 Computational results of C-D anode.

Discussions

Velocity slip

First, comparing exhaust ion velocities (Fig. 13) with exhaust atom velocities (Fig. 14 (a) and Fig. 15 (a)) on the centerline, it is seen that the hydrogen atom velocity relatively small compared with the ion velocity. In this physical phenomenon, namely so-called velocity slip[13], ions are accelerated while neutrals are not. This is undesirable for the following reasons. From an electromagnetic point of view, this so-called atom-ion velocity slip requires the extra power according to the Ohm's law:

$$\mathbf{j} = \sigma\left(\mathbf{E} + \mathbf{u}_i \times \mathbf{B}\right) \tag{13}$$

In the case when only the ions are accelerated, the second term of equation (13) becomes more negative and hence the discharge current tends to further decrease. Thus, in order to keep the discharge current constant, the first term, which is corresponds to the required discharge voltage, must increase and, as a result, extra power is needed. In addition to this extra power requirement, the thrust energy is always greater than kinetic energy of ions and neutrals in the case of velocity slip. In other words, the actual propellant utilization efficiency becomes worse by this selective acceleration.

In order to discuss the velocity slip, the energy balance between ions and neutrals in the discharge chamber must be taken into account. Being accelerated by Lorentz force, ions collide against neutrals. In the high plasma density region, the mean free path of momentum transfer between ions and neutrals is short, and the momentum of the ions is efficiently transferred to neutrals through collisions. However, in the low plasma density region, the momentum of ions does not transferred to neutrals and only ions are accelerated.

In the case of flared anode, toward downstream direction, the atom velocity decreases as shown in Fig. 14 (a) while the ion Mach number increases (Fig 14 (b)). In the vicinity of the cathode tip, where the propellant reaches the maximum speed of 21 km/s and forms a high plasma density region, as shown in Fig.14 (e), and the collision frequency between ions and neutrals is highest. Thus, ion momentum is transferred to neutrals and these neutrals are sufficiently accelerated. However, except for the cathode tip region, the plasma density is low,

thus the neutrals cannot acquire momentum from ions and the neutrals are decelerated.

While in the C-D anode case, both ions and atoms are accelerated downstream. In this configuration, the high plasma density region is wider compared to the flared anode case, and neutrals are accelerated using the energy imparted by the ions. Farther downstream, velocity slip takes place and neutrals are slightly decelerated. Since there is a converging part in the C-D anode, the flow stagnates and decelerates near the cathode tip region.

Estimation of ion temperature and pressure

Using experimental results, we estimated the ion temperature and pressure at the thruster exit on the centerline. The ion temperature was calculated from following equation defining the ion Mach number.

$$M_i = \frac{u_i}{\sqrt{R(\gamma_e T_e + \gamma_i T_i)}} \tag{14}$$

We can estimate the pressure from these two equations. One is the equation of state, and the other is the equation of thrust components:

$$p = kn_e T_i + kn_e T_e + kn_a T_a \tag{15}$$

$$F = \dot{m}_i u_i + \dot{m}_a u_a + pA \tag{16}$$

The estimated results and the atom temperature measured form Doppler broadening of absorption spectrum are given in Table 2. In the case of flared anode, the ion temperature is extremely high compared to the atom temperature. In the C-D anode case, the ion and atom temperature are almost same. We can say that thermal equilibrium between ions and atoms exists, because of the sufficient number of collisions between them. However, it must be noted that both atom and ion temperatures are very high, and this is a main reason for the deterioration in thrust efficiency.

The pressure calculated from this thrust equation is relatively low. This is because the thrust F has been estimated from the average of the exit cross-section, while other values were measured on the centerline (so called cathode jet region) where the discharge energy is concentrated. Considering these facts together, the two estimated pressures are in good agreement.

Due to the high temperatures, the pressure is also high. The momentum thrust and pressure thrust are very similar in their magnitude. Also, the flow is in underexpanded condition, which decreases the thrust level.

Table 2. Estimation of ion temperature and pressure.

	T_i	T_a	p (from eq. (15))	p (from eq. (16))
Flared	14.6 eV	4.5 eV	5.6 kPa	3.1 kPa
C-D	4.4 eV	4.8 eV	5.2 kPa	3.6 kPa

It is assumed that in the C-D anode case the ion temperature and atom temperature are almost same magnitude due to sufficient collision each other. From this assumption of $T_i = T_a$, we can estimate the ion velocity in entire discharge chamber using the equation (14) and the results on the centerline is shown in Fig. 19. The velocity slip is severe especially at the downstream region where plasma density is rarefied.

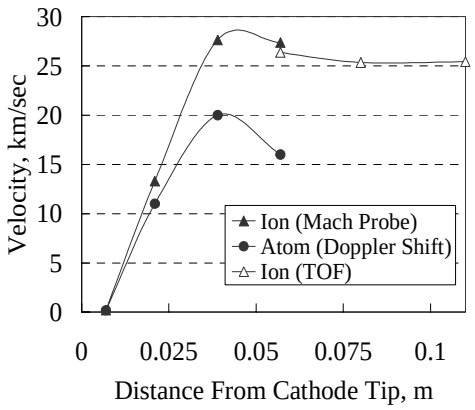

Fig. 19 Comparison of ion and atom velocity in C-D anode.

Estimation of energy flux

Using experimental results and estimations, energy fluxes on the centerline at the thruster exit were calculated for each anode as shown Figs. 20 and 21. Estimated total energy fluxes are relatively higher than the input power because the estimation was conducted on the cathode jet region. Thermal energy loss is highest and cold flow loss of ions, increasing with velocity slip, is also large.

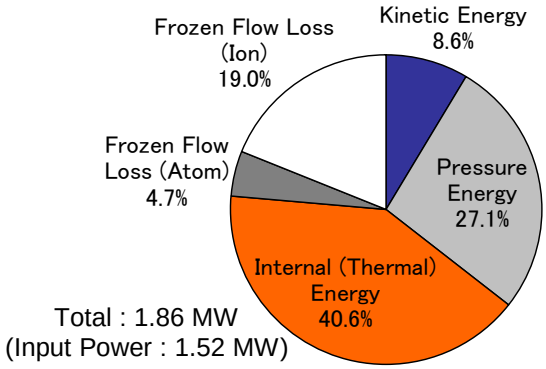

Fig. 20 Energy flux at exit (flared)

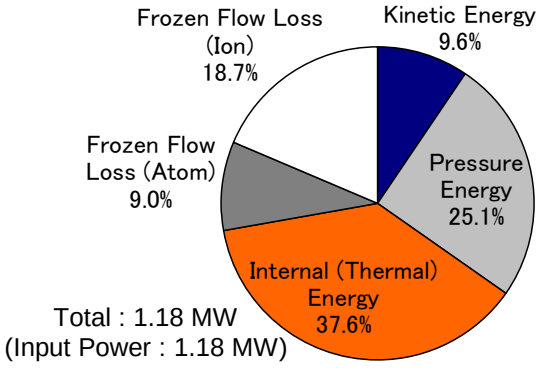

Fig. 21 Energy flux at exit (C-D)

Calculation results

In the flared anode case, the phenomenon of large velocity slip, deceleration of atom at the middle of the anode and non-equilibrium among three temperatures are similar to experimental results. The electron temperature is constant, which is also same as the experiment, because Joule heating is immediately spent as ionization energy. This fact is readily understood from Fig. 22, electron energy balance. The experimental phenomenon the atom temperature becomes minimum at cathode tip and increases at the downstream (as shown Fig. 14 (c)) was also observed in the computation. Figure 23 shows the computational energy balance of atom. From Fig. 23, at the cathode tip region atom temperature is greatly influenced by viscous friction and energy exchange with ion via ionization and collision. At the downstream, the effect of velocity slip friction becomes large. However, the extreme heating of ion is not simulated in this calculation.

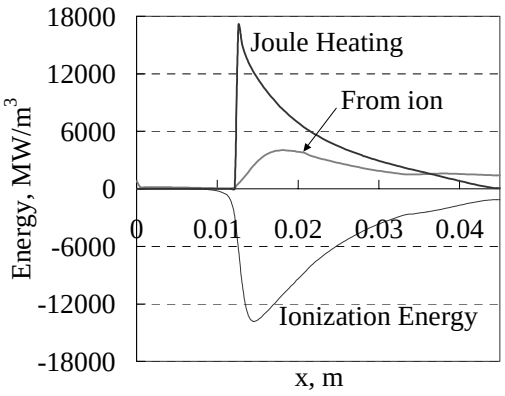

Fig. 22 Computational energy balance of electron.

In the case of C-D anode, less effect of velocity slip is apparent, and in contrast with the flared anode case, neutral atoms do not decelerate. This is because of higher collision coefficient (Fig. 24), which is expressed as following equation:

$$K_{in} = mn_e n_n Q_{in} \overline{C}_i \qquad (17)$$

where Q_{in} is collision cross-section between ion and atom and $\overline{C}_i$ is random velocity of ion. Temperatures of each species are in a similar magnitude and remain low temperature levels compared to experimental values.

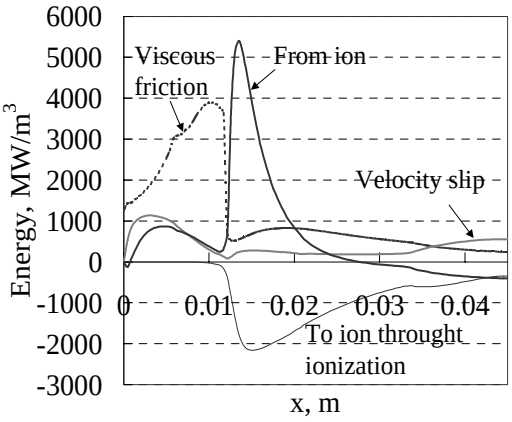

Fig. 23 Computational energy balance of atom.

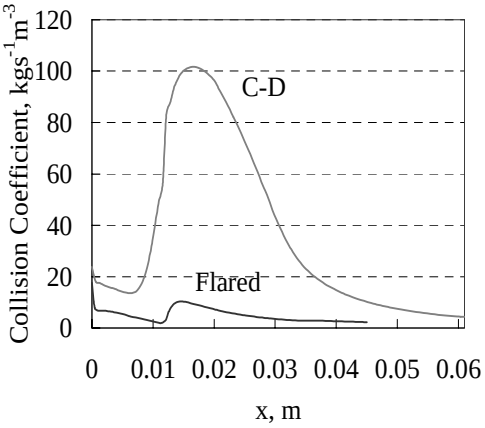

Fig. 24 Comparison of computational collision coefficient.

Concerning Lorentz force distributions, in the case of flared anode, the larger blowing force accelerates ions in entire discharge chamber. In the case of C-D anode, the blowing force almost equals to zero at the middle of diverging part. However, the pumping force becomes very large especially at the region between the cathode tip and the throat. This phenomenon causes promotion of the plasma generation and efficient momentum transfer from ions to atoms. From these facts, we can say that electromagnetic acceleration is dominant in flared anode and C-D anode realizes efficient acceleration of atoms. Figure 24 shows the thruster performance for both anodes under the condition mass flow rate is same as our experiment[14]. At the high Isp operation flared anode is superior, however, at the low Isp operation C-D anode is more efficient.

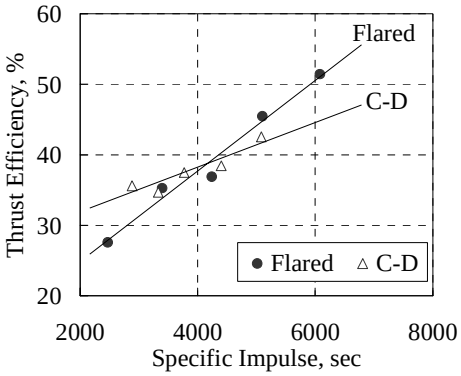

Fig. 25 Comparison of thrust performance ($\dot{m} = 0.65$g/s).

Conclusions

Some experiments and numerical calculation for a 2D-MPD arcjet using two types of anodes were conducted. Atom velocities were estimated using laser absorption spectroscopy and ion velocities were estimated using TOF and Mach probe method. The experimental results revealed that the ions are accelerated sufficiently, but atoms are not relatively large portion of the discharge chamber. The reason can be found in the fact that atom-ion collisions, or momentum transfer, are insufficiently and results in velocity slip between ions and atoms. This velocity slip phenomenon decreases the thrust efficiency. Also, measured temperature levels were found to be extremely high and this is considered to be another reason for low thrust efficiency in MPD arcjets. Comparing results for the two different anode configurations, the converging-diverging anode enabling higher plasma density was found to yield high thrust performance due to the efficient momentum transfer between atoms and ions at low Isp operation, while at high Isp operation a simple flared anode might be better.

References

[1] Toki, K., Shimizu, Y., and Kuriki, K., "Electric Propulsion Experiment (EPEX) of a Repetitively Pulsed MPD Thruster System Onboard Space Flyer Unit (SFU)," 25th IEPC, Paper 97-120, 1997.
[2] Suzuki, H., Uematsu, K. and Kuriki, K., "Endurance Test of Fast Acting Valve," AIAA Paper 85-2058, 1985.
[3] Kurik, K., Shimizu, Y., Yoshida, T., Gohnai, T., Harada, H. and Obara, H., "Power Supply Unit for MPD Thruster," 17th IEPC, Paper 84-26, 1984.
[4] Mellon, M. G., *Analytical Absorption Spectroscopy*, John Wiley & Sons, New York, 1965.
[5] Griem, H. R., *Spectral Line Broadening by Plasma*, Academic Press, 1974.
[6] Lochte-Holtgreven, W., *Plasma Diagnostics*, AIP Press, 1968
[7] Kinefuchi. K., MSc Thesis, University of Tokyo, 2003.
[8] Ando, A., Hattori, K., Inutake, M., Sugimura, T., Hori, F., Fukushi, K., Ochiai, T., Yamamoto, M., Yagai, T., Imasaki, A. and Yoshimura, M., "Mach-probe Characteristics in a Magnetized Plasma Flow," 26th IEPC, Paper 99-180, 1999.
[9] Stangeby, P. C. and Allen, J. E., "Transonic Plasma Flow Past an Obstacle," J. Plasma Phys., Vol. 6, Part 1, 1971, pp. 19-32.
[10] Swift, J. D. and Schwar, M. J. R., *Electrical Probes for Plasma Diagnostics*, Iliffe Books, London, 1970.
[11] Jahn, R. G., Clark, K. E., Oberth, R. C. and Turchi P. J., "Acceleration Patterns in Quasi-Steady MPD Arcs," AIAA J., Vol. 9, No. 1, 1971, pp. 167-172.
[12] Niewood, E. H. and Martinez-Sanchez, M., "Quasi-One-Dimensional Numerical Simulation of Magnetoplasmadynamic Thrusters," J. Prop. & Power, Vol. 8, No. 5, 1992, pp. 1031-1039.
[13] Malliaris, A. C. and Libby D. R., "Spectroscopic Study of Ion-Neutral Coupling in Plasma Acceleration," AIAA J., Vol. 9, No. 1, 1971, pp. 160-167.
[14] Funaki, I., Toki, K. and Kuriki, K., "Electrode Configuration Effect on the Performance of a Two-Dimensional Magnetoplasmadynamic Arcjet," J. Prop. & Power, Vol. 14, No. 6, 1998, pp. 1043-1048.